APL Photonics

Second harmonic generation in strained transition metal dichalcogenide monolayers: MoS_2, $MoSe_2$, WS_2, and WSe_2

Cite as: APL Photonics **4**, 034404 (2019); https://doi.org/10.1063/1.5051965
Submitted: 13 August 2018 . Accepted: 05 November 2018 . Published Online: 12 December 2018

Lukas Mennel, Matthias Paur, and Thomas Mueller

COLLECTIONS

Paper published as part of the special topic on Nonlinear Optics in 2D Materials

EP This paper was selected as an Editor's Pick

View Online Export Citation CrossMark

ARTICLES YOU MAY BE INTERESTED IN

Nonlinear optics in carbon nanotube, graphene, and related 2D materials
APL Photonics **4**, 034301 (2019); https://doi.org/10.1063/1.5051796

Nonlinear plasmonics of three-dimensional Dirac semimetals
APL Photonics **4**, 034402 (2019); https://doi.org/10.1063/1.5042450

Intraband divergences in third order optical response of 2D systems
APL Photonics **4**, 034201 (2019); https://doi.org/10.1063/1.5053715

AMERICAN ELEMENTS
THE ADVANCED MATERIALS MANUFACTURER®
American Elements opens up a world of possibilities so you can **Now Invent!**
Over 15,000 certified high purity laboratory chemicals, metals, & advanced materials and a state-of-the-art Research Center. Printable GHS-compliant Safety Data Sheets. Thousands of new products. And much more. All on a secure multi-language "Mobile Responsive" platform.
Now Invent.™
The Next Generation of Material Science Catalogs
www.americanelements.com

© 2018 Author(s).

Second harmonic generation in strained transition metal dichalcogenide monolayers: MoS_2, $MoSe_2$, WS_2, and WSe_2

Cite as: APL Photonics 4, 034404 (2019); doi: 10.1063/1.5051965
Submitted: 13 August 2018 • Accepted: 5 November 2018 •
Published Online: 12 December 2018

View Online Export Citation CrossMark

Lukas Mennel,[a] Matthias Paur, and Thomas Mueller[a]

AFFILIATIONS

Institute of Photonics, Vienna University of Technology, Gußhausstraße 27-29, 1040 Vienna, Austria

[a]Authors to whom correspondence should be addressed: lukas.mennel@tuwien.ac.at and thomas.mueller@tuwien.ac.at

ABSTRACT

Second-harmonic generation (SHG) is a powerful measurement technique to analyze the symmetry properties of crystals. Mechanical strain can reduce the symmetry of a crystal and even weak strain can have a considerable impact on the SHG intensity along different polarization directions. The impact of strain on the SHG can be modeled with a second-order nonlinear photoelastic tensor. In this work, we determined the photoelastic tensors at a fundamental wavelength of 800 nm for four different transition metal dichalcogenide (TMD) monolayers: MoS_2, $MoSe_2$, WS_2, and WSe_2. Strain is applied using a three-point bending scheme, and the polarization-resolved SHG pattern is measured in backscattering geometry. Furthermore, we connected the strain dependent SHG with the strain dependence of the A-exciton energy. With the second-order nonlinear photoelastic tensor, full strain information can be accurately extracted from polarization-resolved SHG measurements. Accordingly, uniaxial strain, induced by polydimethylsiloxan (PDMS) exfoliation and transfer, is measured. We find that TMD monolayers fabricated with PDMS are strained by ~0.2%. With the experimentally determined nonlinear photoelastic tensors, it will be possible to optically probe arbitrary strain fields in TMD monolayers.

© 2018 Author(s). *All article content, except where otherwise noted, is licensed under a Creative Commons Attribution (CC BY) license (http://creativecommons.org/licenses/by/4.0/).* https://doi.org/10.1063/1.5051965

I. INTRODUCTION

The availability of highly intense light, made possible by the development of short-pulse lasers, has allowed for the investigation of nonlinear optical processes.[1] There is a wide range of nonlinear optical effects, spanning from frequency mixing[2] to the optical Kerr effect.[3] The first discovered nonlinear optical effect is second-harmonic generation (SHG),[1] which has, together with the related phenomena of sum- and difference-frequency generation, many important applications. These effects are used, for example, in optical parametric oscillators,[4] in quantum optics to generate entangled photons,[5] or to produce femtosecond light pulses by Kerr-lens mode-locking.[6] Symmetry plays a key role in nonlinear optics.[7] SHG can (within the electric dipole approximation) only occur in materials without an inversion center. On the other hand, odd-ordered nonlinear processes, such as third-harmonic generation (THG), are allowed in all materials.

Since the discovery of graphene in 2004, many other materials with a stable monolayer form have been found,[8] including the important subclass of transition metal dichalcogenides (TMDs). TMDs are centrosymmetric in their bulk form, but if thinned down to monolayer thickness, they lack this symmetry. TMDs in two-dimensional (2D) form possess unique physical properties, and numerous properties arise from broken inversion symmetry, including circular dichroism,[9] ferroelectricity,[10] piezoelectricity,[11] and pyroelectricity.[10] From a nonlinear optics viewpoint, the enormous second-order nonlinear susceptibility $\chi_0^{(2)}$ of TMD monolayers gives rise to efficient frequency conversion without the requirement for phase-matching. The weak dielectric screening in atomically thin crystals[12] greatly enhances the Coulomb

© Author(s) 2018

interaction between electrons and holes and thus the matrix elements of optical transitions. Therefore, the nonlinear susceptibility $\chi_0^{(2)}$ of TMDs has an absolute value of a few nm/V which is orders of magnitude larger than that for common nonlinear crystals.[13–15] Due to the two-dimensional nature of TMDs, some authors proposed a sheet nonlinear susceptibility which has a magnitude of 10^4 pm^2/V for a MoS_2 monolayer.[14,16,17] In recent years, many interesting nonlinear optical studies have been conducted. For example, SHG has been used to determine the crystal lattice orientation in order to align the lattices of different TMDs in heterostructures.[18] SHG has also been used to detect edge states in MoS_2[19] and to image grains and grain boundaries in polycrystalline films.[20] TMD monolayers can sustain very high levels of mechanical strain,[21] allowing them to be bent and implemented in flexible (opto-)electronic devices. Under strain, the electrical and optical properties of the materials are altered. In TMDs, strain tunes the bandgap,[22] Raman modes are shifted,[23] exciton-phonon coupling is modulated,[24] and excitons are funneled along strain gradients.[25] Single photon emission from TMDs is also closely connected to strain.[26–31] Furthermore, as in silicon,[32] strain engineering can be employed in TMDs to increase the carrier mobility.[33,34] Recently, it has been shown that strain has an immense influence on the SHG response in TMDs.[35,36] This effect can be used to measure high-resolution strain maps. With a precise model and measurements of how strain affects the SHG in different materials, optimized nonlinear optical devices can be built via strain engineering. In this work, we investigate the influence of strain on SHG in the four semiconducting TMDs that are stable in atmosphere and at room temperature, namely, MoS_2, $MoSe_2$, WS_2, and WSe_2.[37]

II. THEORETICAL DESCRIPTION

Within the dipole approximation, the polarization of a material can be expressed as a power series $\mathbf{P}_i \propto \chi_{ij}^{(1)}\mathbf{E}_j + \chi_{ijk}^{(2)}\mathbf{E}_j\mathbf{E}_k + \chi_{ijkl}^{(3)}\mathbf{E}_j\mathbf{E}_k\mathbf{E}_l + \cdots$.[7] The induced polarization $\mathbf{P}_i$ is determined by the susceptibility coefficients $\chi^{(n)}$ and the applied electric field vector components $\mathbf{E}_i$. The susceptibility coefficients $\chi^{(n)}$ are tensors of rank $n+1$ and are highly symmetry dependent. In centrosymmetric materials, all even ordered susceptibility components vanish. Furthermore, the susceptibility tensor components reflect the symmetries of the underlying crystal structure. This allows structural investigations via nonlinear optical processes. The frequencies of the applied electric field vectors mix in these nonlinear optical processes, and therefore, the contributions of the different processes can be distinguished spectroscopically. The lowest order nonlinear optical process is a three-wave mixing process. If the incident electric fields have the same frequency, it is called second-harmonic generation. In a SHG process, two photons of the same frequency are converted into a single photon with twice that frequency

$$\mathbf{P}_i^{(2)}(2\omega) \propto \chi_{ijk}^{(2)}\mathbf{E}_j(\omega)\mathbf{E}_k(\omega). \tag{1}$$

TMD monolayer crystal lattices in the 2H phase belong to the trigonal prismatic (D_{3h}) point group. Considering this symmetry, the second-order nonlinear susceptibility tensor $\chi_{ijk}^{(2)}$ has four non-zero elements with one free parameter $\chi_0^{(2)}$.[38] Exciting the TMD monolayer with linear polarized light under normal incidence and then filtering the SHG response with a linear polarizer, oriented along the fundamental polarization angle ϕ, results in a six-fold SHG intensity pattern $I_{\parallel}^{(2)} \propto \cos(3\phi - 3\delta)^2$, where the angle δ is the rotation of the armchair direction of the crystal relative to the x-axis. The maxima of the polarization-resolved SHG response coincide with the armchair directions of the TMD lattice, as illustrated in Fig. 1(f). This allows the determination of the lattice orientation of TMD crystals.

Strain can break the crystal symmetry and therefore change the nonlinear susceptibility tensor. In order to mathematically describe the influence of strain, a photoelastic tensor $\mathbf{p}_{ijklm}$ of fifth rank is introduced. This tensor translates the strain tensor $\mathbf{u}_{lm}$ linearly into a contribution to the nonlinear susceptibility tensor of the unstrained crystal $\chi_{ijk}^{(2,0)}$ and is defined as $\mathbf{p}_{ijklm} = \partial\chi_{ijk}^{(2,0)}/\partial\mathbf{u}_{lm}$. The total nonlinear susceptiblity $\chi_{ijk}^{(2)}$, including the strain contribution, is then given as[39]

$$\chi_{ijk}^{(2)} = \chi_{ijk}^{(2,0)} + \mathbf{p}_{ijklm}\mathbf{u}_{lm}. \tag{2}$$

The photoelastic tensor reflects the crystal symmetries, the symmetry of the strain tensor ($\mathbf{u}_{lm} = \mathbf{u}_{ml}$), and the symmetry of the SHG process ($\chi_{ijk}^{(2)} = \chi_{ikj}^{(2)}$). Under these conditions, it reduces to 12 nonzero elements with two free parameters, p_1 and p_2,[35,38]

$$\begin{aligned} &p_{xxxxx} = p_1, \quad p_{xxxyy} = p_2, \quad p_{xyyyy} = -p_1, \quad p_{xyyxx} = -p_2, \\ &p_{yyxyy} = p_{yyxxx} = p_{yxyyy} = p_{yxyxx} = -\frac{1}{2}(p_1 + p_2), \\ &p_{yyyyx} = p_{yyyxy} = p_{yxxyx} = p_{yxxxy} = -\frac{1}{2}(p_1 - p_2). \end{aligned} \tag{3}$$

The two-dimensional strain tensor can be rotated by an angle θ in a way that the shear strain elements (u_{xy}, u_{yx}) become zero. The strain angle θ is given relative to the x-axis and thus independent of the crystal orientation. Under consideration of Poisson's ratio ν, we then get the two principal strain tensor elements $u_{xx} = \varepsilon_{xx} - \nu\varepsilon_{yy}$ and $u_{yy} = \varepsilon_{yy} - \nu\varepsilon_{xx}$.

By combining Eqs. (1) and (2) and calculating the parallel polarization-resolved SHG response, the strain dependent SHG intensity at the polarization direction φ is

$$I_{\parallel}^{(2)}(2\omega) \propto (\mathrm{A}\cos(3\varphi - 3\delta) + \mathrm{B}\cos(2\theta + \varphi - 3\delta))^2, \tag{4}$$

with $\mathrm{A} = (1-\nu)(p_1 + p_2)(\varepsilon_{xx} + \varepsilon_{yy}) + 2\chi_0^{(2)}$ and $\mathrm{B} = (1+\nu)(p_1 - p_2)(\varepsilon_{xx} - \varepsilon_{yy})$. The first part of Eq. (4), with pre-factor A, depends on the sum of the two strain elements ε_{xx} and ε_{yy} and changes the nonlinear susceptibility tensor element of the unstrained crystal $\chi_0^{(2)}$ directly. This term has the same φ-dependence as the SHG of the unstrained crystal and therefore only

© Author(s) 2018

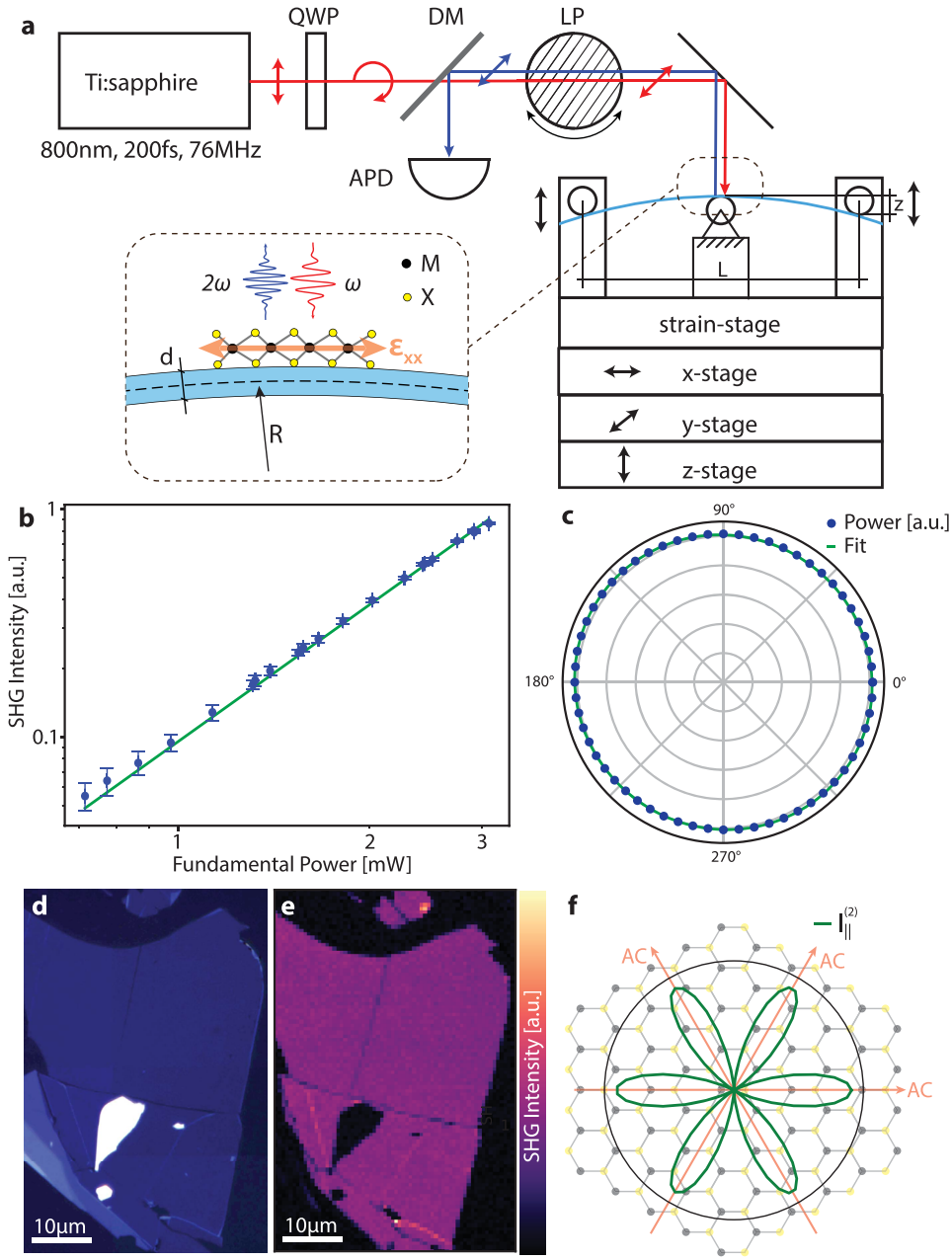

FIG. 1. (a) Schematic illustration of the optical SHG setup and three-point bending stage. The enlarged view schematically shows the SHG process in a strained TMD monolayer. QWP: quarter wave plate, DM: dichroic mirror, LP: linear polarizer, d: sample thickness, R: bending radius, and ε_{xx}: uniaxial strain. (b) Power dependence of the SHG intensity. (c) Azimuthal power distribution of the fundamental. (d) Optical microscope image of a MoS_2 monolayer. (e) SHG intensity map of the corresponding MoS_2 monolayer flake. (f) Sketch of the polarization-resolved SHG intensity in connection with the underlying crystal geometry.

changes the SHG amplitude. The second term, with pre-factor B, depends on the difference of the principal strain components ε_{xx} and ε_{yy}. This implies that if the crystal is strained purely biaxial ($\varepsilon_{xx} = \varepsilon_{yy}$), the B-term vanishes. Only if the symmetry is broken by strain, the B-part of the equation becomes nonzero, resulting in a symmetry-breaking of the SHG intensity pattern along the principal strain tensor angle θ. The way how the second-harmonic (SH) response changes with strain is described by the sum and difference of the photoelastic tensor parameters p_1 and p_2. These parameters are material specific and are determined experimentally in this work.

III. SHG SETUP AND SAMPLE FABRICATON

Figure 1(a) shows a schematic of our polarization-resolved SHG setup, which measures the parallel polarization intensity $I_{\parallel}^{(2)}$ of the emitted SH light. A Ti:sapphire laser source is

© Author(s) 2018

used to produce 200 fs pulses at 800 nm wavelength. Using a quarter wave plate (QWP), the linearly polarized light from the laser is converted into circularly polarized light. The light then passes through a dichroic mirror (DM) and a linear polarizer (LP), mounted in a rotation stage to set the excitation polarization angle φ. Using a 100× microscope objective, the light is focused onto the sample and the SHG signal is collected by the same objective and passed through the same polarization filter (LP). The DM splits the fundamental from the SH light component. Band- and short-pass filters further suppress the fundamental part of the light before the SH response is detected with an avalanche photodiode (APD). The measured quadratic power dependence of the SHG process is shown in Fig. 1(b). For polarization-resolved measurements, the LP is rotated in 6° steps over a full turn and the SH intensity is detected at each step. It is crucial to ensure that the fundamental power is constant when the LP is rotated, as a power variation with the polarization angle drastically influences the SH response. By careful alignment using a polarimeter, we could minimize the power variation to less than 2% [Fig. 1(c)]. Even though the power variation is small, we fit the measurement data with an ellipse and correct the SH data with that fit. Since the polarization purity is so crucial, we detect the power variation before each SHG measurement series.

In order to apply uniaxial strain to the TMD monolayers, we employ a three-point bending technique,[40] using 0.25 mm thick polyethylene naphthalate (PEN) flexible substrates. An ~5 μm thick layer of SU-8 (MicroChem) is spun onto the PEN substrates and is hard-baked at 200 °C for 30 min. This planarizes the polymer surface and, due to cross-linking in the hard-baking step, the SU-8 layer gains high mechanical strength while maintaining its ductility.[41] TMD monolayers are mechanically exfoliated using polydimethylsiloxan (PDMS, GelPak) and identified with an optical microscope. Using a dry transfer technique,[42] the TMD monolayers are then placed at the center of the PEN/SU-8 substrates.

A schematic of our three-point bending setup is shown in Fig. 1(a). The middle rod is fixed and the two side rods can move vertically. The flexible substrate is placed on top of the middle rod and below the two side rods. As the side rods move down, the flexible substrate becomes bent. In order to minimize the lateral forces, and thereby a movement of the substrate during the bending process, the side rods are fixed with ball bearings. Thus, little to no lateral readjustment of the focus point is needed when the sample is probed at different strain levels. The bending setup is mounted on an xy-stage, which allows spatial mapping of the SHG signal. In Fig. 1(d), a micrograph of a MoS_2 monolayer is shown and the corresponding SHG intensity map is plotted in Fig. 1(e). The applied uniaxial strain is calculated from the bending geometry. Tensile strain on top of the substrate depends on the substrate thickness d and the bending radius R

$$\varepsilon_{xx} = \frac{d}{2R}. \tag{5}$$

The bending radius R is calculated geometrically. The distance L of the side rods is 20 mm, and the vertical distance z of the side rods relative to the neutral point is set by the strain-stage. This results in the following relation for the applied strain:

$$\varepsilon_{xx} = \frac{4zd}{4z^2 + L^2}. \tag{6}$$

We also conducted strain dependent photoluminescence (PL) measurements by using the same three-point bending technique used in the SHG experiments. In these measurements, the TMD monolayers were excited with a 532 nm continuous-wave laser and the PL signal was analyzed with a grating spectrometer and a silicon CCD.

IV. EXPERIMENTAL RESULTS

The photoelastic coefficients p_1 and p_2 for the relevant TMD monolayers were determined by applying varying levels of strain and measuring the polarization-resolved SHG. In order to avoid slipping of the TMD monolayer on the bent substrate, we limited the applied strain to values below 0.5%. In Figs. 2(a)–2(d), polarization-resolved SHG measurements are plotted for the lowest and highest applied strain levels for the different TMD materials. We fit the measured data with Eq. (4), where A, B, and θ are the free parameters, using the *curve_fit* method of the *SciPy* package.[43] The errors of the fit parameters are numerically estimated by an algorithm that considers measurement errors. The so obtained fits of the SHG measurements with varying strain are plotted in Figs. 2(e)–2(h). SHG fits with measurement points and errors are illustrated in Figs. 2(a)–2(d), where the validity of the fitting process is apparent. By applying uniaxial strain in two perpendicular directions (i.e., by rotating the samples by 90°), we confirmed the prediction of the photoelastic tensor theory that there is no difference between strain along the armchair and zig-zag directions of the TMD crystal [Figs. 2(i)–2(l)].

Figure 3 shows the fit parameters as extracted from the strain dependent SHG measurements. From Eq. (4), it is apparent that the nonlinear susceptibility $\chi_0^{(2)}$ of the unstrained crystal affects the fitting procedure. An accurate measurement of the absolute $\chi_0^{(2)}$-value is not trivial–especially in backscattering geometry–and reported values in the literature diverge widely for TMD monolayers. We therefore present the parameters A and B normalized by $\chi_0^{(2)}$ of the respective TMD materials. This normalization also allows for a direct comparison of the relative influence of strain on the SHG patterns in different materials. The (setup-dependent) proportionality factor that relates the measured SHG signal to the right-hand side of Eq. (4) is then simply determined by performing a calibration measurement on an unstrained sample: $I_{\parallel}^{(2)}(2\omega) \propto \left(A(\varepsilon_{xx} = \varepsilon_{yy} = 0)/\chi_0^{(2)} \cos(3\varphi - 3\delta)\right)^2$ with $A(\varepsilon_{xx} = \varepsilon_{yy} = 0)/\chi_0^{(2)} = 2$. After calibration, only the relative magnitudes between

© Author(s) 2018

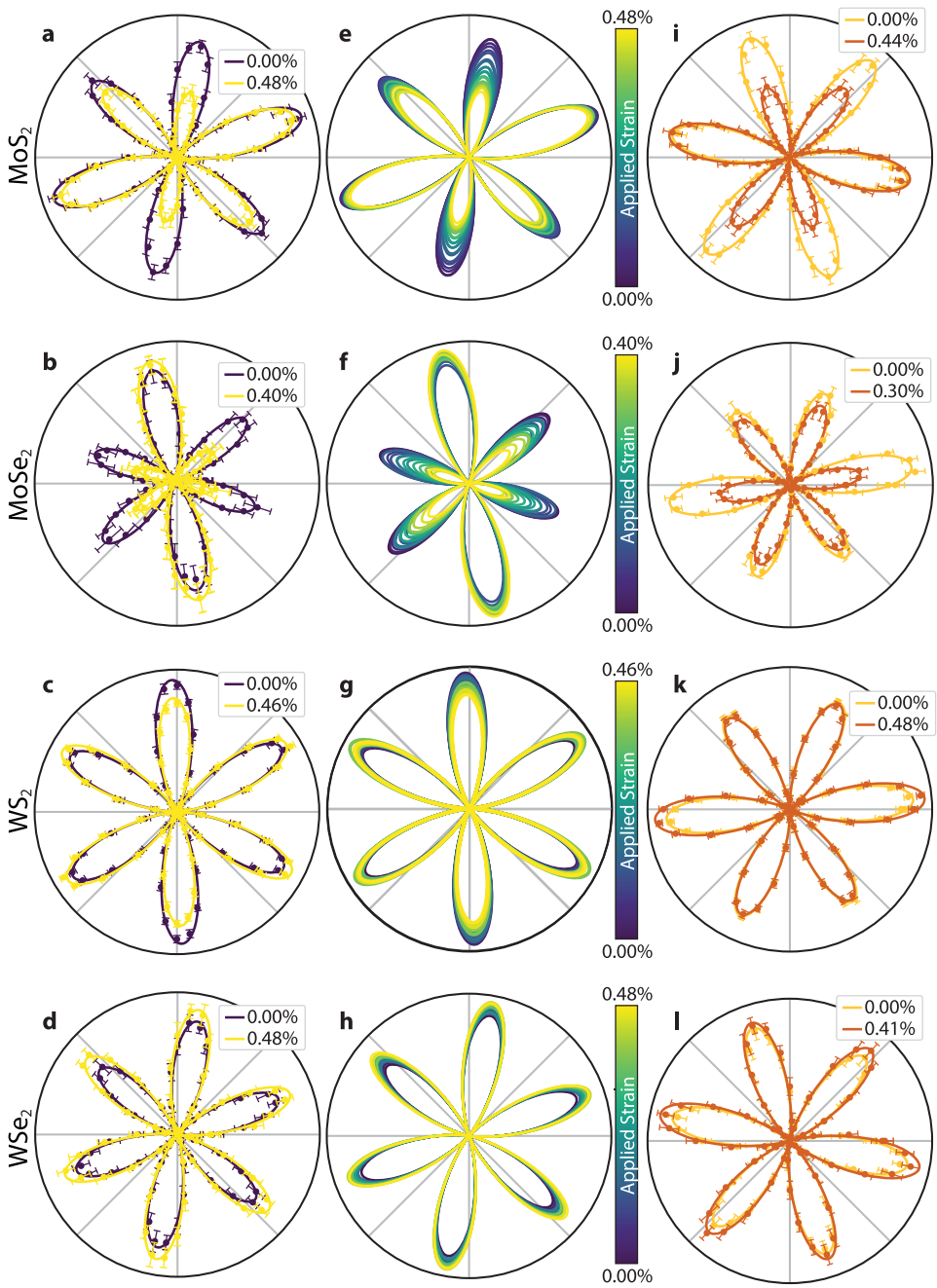

FIG. 2. Polarization-resolved SHG measurements of MoS_2, $MoSe_2$, WS_2, and WSe_2, under varying applied strain levels. Uniaxial strain was applied along the horizontal axis. [(a)–(d)] SHG measurements at the lowest and highest applied strain levels. [(e)–(h)] Fitted SHG curves at various applied strain levels. [(i)–(l)] SHG measurements at two different strain levels where the samples are rotated by 90° with respect to the SHG measurements on the left. Symbols: measurement data; lines: fits.

the photoelastic tensor elements and nonlinear susceptibility are required in order to measure strain with polarization-resolved SHG. In Table I, the numerical values of the relative magnitude of the nonlinear susceptibility parameters $\chi_0^{(2)}$ are listed.

In most of our samples, the six-fold SHG symmetry is broken even without externally applied strain. The symmetry breaking depends on the sample orientation (verified by rotating the samples by 90°), which excludes the measurement setup as cause. It has been reported that exfoliation and transfer with PDMS can cause strain in TMD samples.[44] We therefore attribute the symmetry breaking to a strain caused by the exfoliation and transfer process. We refer to this preexisting strain as initial strain ε_i, and it has to be considered when extracting the photoelastic tensor parameters. In order

© Author(s) 2018

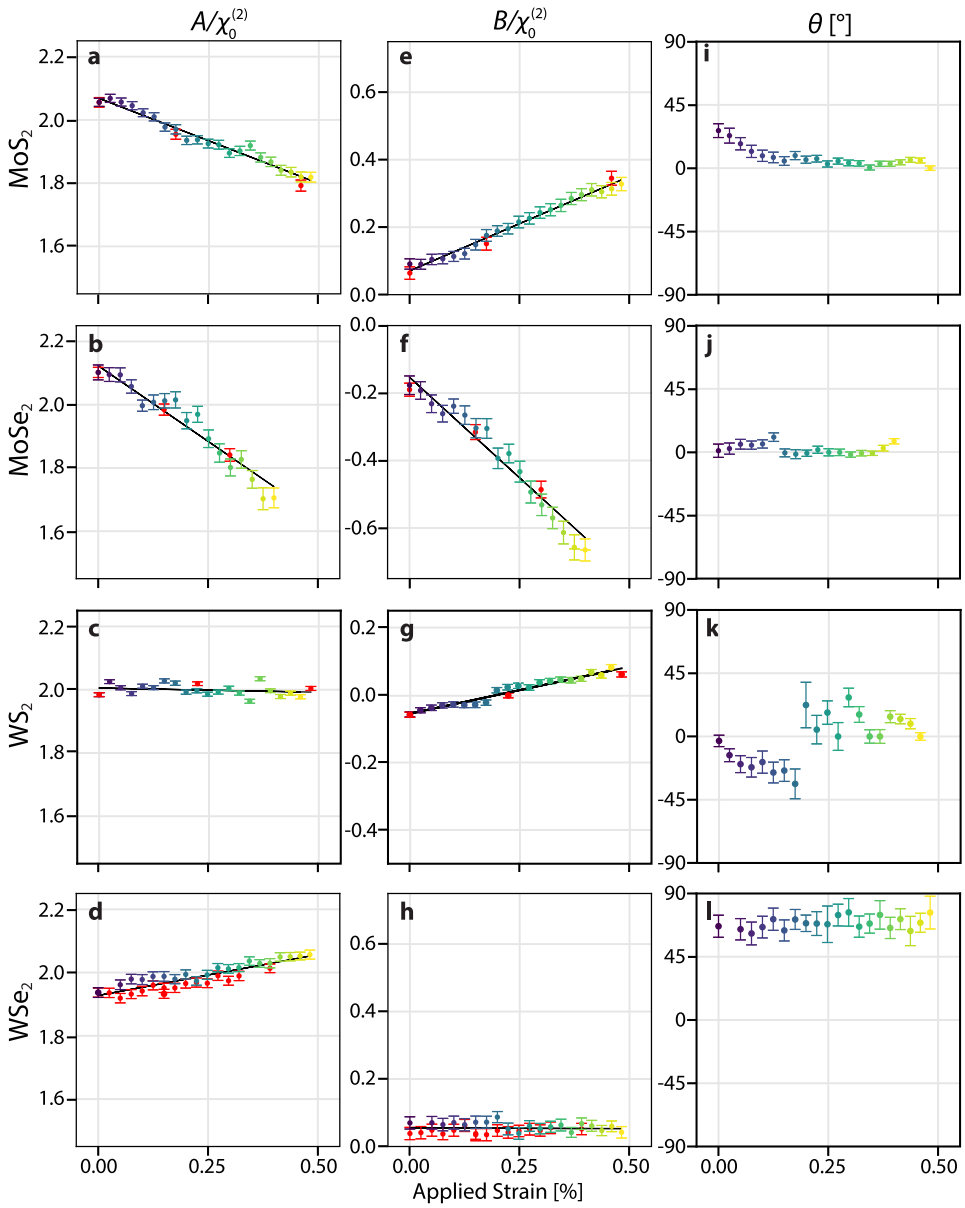

FIG. 3. Fit parameters of the strain dependent SHG measurements for MoS_2, $MoSe_2$, WS_2, and WSe_2. The color gradient corresponds to the colors from Figs. 2(e)–2(h). Fit parameters represented by red color are measurements when the sample was rotated by 90°. [(a)–(d)] Fit parameter A divided by the nonlinear susceptibility of the unstrained crystal $\chi_0^{(2)}$. [(e)–(h)] Fit parameter B divided by $\chi_0^{(2)}$. [(i)–(l)] Fit parameter θ in degrees. Strain is applied along 0°.

to quantify the initial strain, we assume, for now, that it is uniaxial and compressive—the validity of this assumption will be demonstrated later. Furthermore, we apply the external strain in either a parallel or perpendicular direction to the initial strain coordinate system. Under these conditions, we are able to determine the initial strain and we can normalize parameters A and B accordingly. The following relations give the initial strain for parallel and perpendicular orientations of the applied and initial strain, respectively, $\varepsilon_i = -\varepsilon_{xx}|_{B=0}$ and $\varepsilon_i = \varepsilon_{xx}|_{B=0}$. In order to obtain the fit parameters in normalized form, we multiply the A and B by $2/(A(\varepsilon_{xx} = 0) - \varepsilon_i\, \partial A/\partial \varepsilon_{xx})$, which ensures that $A(\varepsilon_{xx} + \varepsilon_i = 0)/\chi_0^{(2)} = 2$.

The $A/\chi_0^{(2)}$ and $B/\chi_0^{(2)}$ data points in Fig. 3 show a distinct linear dependence on the applied strain. Due to the initial strain, the B-parameter, at zero applied strain, switches sign when the sample is rotated by 90°. For direct comparison, we thus mirrored the $B/\chi_0^{(2)}$ data points of the rotated samples (red color) in Fig. 3, twice: first horizontally along the value of $B(\varepsilon_{xx} = 0)/\chi_0^{(2)}$ and a second time along the abscissa. This operation compensates the sign change of the B-parameter for the measurements of the rotated samples. The gradients of the $A/\chi_0^{(2)}$ and $B/\chi_0^{(2)}$ fit parameters are obtained by linear fitting and are listed in Table I. With this, we can calculate the photoelastic parameters

© Author(s) 2018

TABLE I. Numerical values of relevant material parameters: $\chi_0^{(2)}/\chi_{0,\mathrm{MoS_2}}^{(2)}$: normalized second-order nonlinear susceptibility; $\chi_0^{(2)}$: second-order nonlinear susceptibility; ν: Poisson's ratio; $\partial \mathrm{A}/\partial\varepsilon_{xx}$: gradient of the SHG fit parameter A; $\partial \mathrm{B}/\partial\varepsilon_{xx}$: gradient of the SHG fit parameter B; p_1, p_2: nonlinear second-order photoelastic tensor elements; $\partial \mathrm{E}_g/\partial\varepsilon_{xx}$: strain dependent A-exciton peak gradient.

	MoS_2	$MoSe_2$	WS_2	WSe_2
$\chi_0^{(2)}/\chi_{0,\mathrm{MoS_2}}^{(2)}$	1	0.82	1.66	1.74
ν	0.25[45,46]	0.23[45]	0.22[45,47]	0.19[45]
$\frac{1}{\chi_0^{(2)}}\frac{\partial \mathrm{A}}{\partial\varepsilon_{xx}}$	−0.54 ± 0.02	−0.96 ± 0.06	−0.03 ± 0.03	0.26 ± 0.02
$\frac{1}{\chi_0^{(2)}}\frac{\partial \mathrm{B}}{\partial\varepsilon_{xx}}$	0.56 ± 0.02	−1.12 ± 0.06	0.28 ± 0.02	−0.003 ± 0.017
$\frac{p_1}{\chi_0^{(2)}}$ (1/%)	−0.13 ± 0.02	−1.10 ± 0.05	0.10 ± 0.02	0.160 ± 0.015
$\frac{p_2}{\chi_0^{(2)}}$ (1/%)	−0.58 ± 0.02	−0.14 ± 0.05	−0.13 ± 0.02	0.162 ± 0.015
$\frac{\partial \mathrm{E}_g}{\partial\varepsilon_{xx}}$ (meV/%)	...	−54.8 ± 5.8	−61.2 ± 3.8	−53.0 ± 3.1
$\frac{p_1}{\chi_0^{(2)}}/\frac{\partial \mathrm{E}_g}{\partial\varepsilon_{xx}}$ (1/eV)	...	20.0 ± 2.3	−1.6 ± 0.3	−3.0 ± 0.3
$\frac{p_2}{\chi_0^{(2)}}/\frac{\partial \mathrm{E}_g}{\partial\varepsilon_{xx}}$ (1/eV)	...	2.5 ± 0.9	2.1 ± 0.3	−3.0 ± 0.3

from

$$\frac{p_1}{\chi_0^{(2)}} = \frac{1}{2}\left(\frac{1}{(1-\nu)}\frac{\partial \mathrm{A}/\chi_0^{(2)}}{\partial\varepsilon_{xx}} + \frac{1}{(1+\nu)}\frac{\partial \mathrm{B}/\chi_0^{(2)}}{\partial\varepsilon_{xx}}\right),$$
$$\frac{p_2}{\chi_0^{(2)}} = \frac{1}{2}\left(\frac{1}{(1-\nu)}\frac{\partial \mathrm{A}/\chi_0^{(2)}}{\partial\varepsilon_{xx}} - \frac{1}{(1+\nu)}\frac{\partial \mathrm{B}/\chi_0^{(2)}}{\partial\varepsilon_{xx}}\right). \tag{7}$$

In Table I, the numerical values of the photoelastic tensor elements and other parameters of the investigated TMD materials can be found.

We also determined the strain induced A-exciton shift, using the same samples as for the SHG measurements. In Figs. 4(a)–4(c), the PL spectra for varying applied strain levels are plotted. The A-exciton peak undergoes a redshift when the TMD flake is under tensile strain.[24] The yellow curves in subplots 4(a)–4(c) correspond to zero strain after the applied strain is released. Subplots 4(d)–4(f) show the fitted A-exciton peaks of the corresponding TMD flakes. Due to the strong PL of the SU-8 layer beneath the TMD flakes, we were not able to detect the PL from the MoS_2 sample. The fitted strain induced A-exciton peak shifts $\partial \mathrm{E}_g/\partial\varepsilon_{xx}$ are listed in Table I.

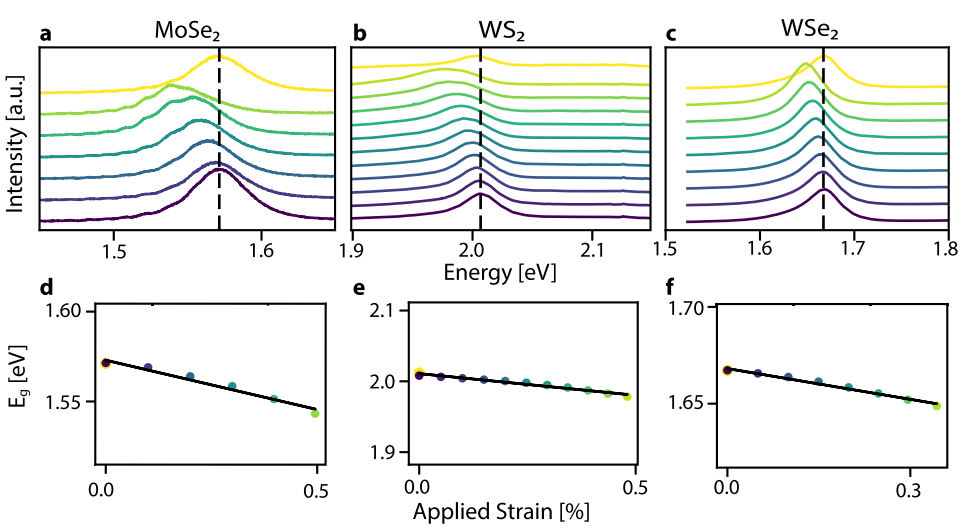

FIG. 4. [(a)–(c)] PL measurements under varying applied strain for $MoSe_2$, WS_2, and WSe_2 respectively (symbols: measurement data; dashed line: unstrained A-exciton peak position). [(d)–(f)] Fitted A-exciton peak position of the corresponding PL measurements. E_g is the A-exciton energy (symbols: fitted A-exciton position; line: fit of the A-exciton shift). The color of the PL measurement corresponds to the strain level of the A-exciton peak fit.

© Author(s) 2018

V. DISCUSSION

In our analysis above, we have assumed the initial strain to be purely uniaxial and compressive. We calculate initial strain values of −0.15%, −0.18%, and −0.22% for MoS_2, $MoSe_2$, and WS_2, respectively. The PL measurements indicate that the initial strain is indeed compressive, as the A-exciton peaks at zero applied strain are blue-shifted, which is relative to the typically reported A-exciton peak energies. The strain corresponding to the initial A-exciton blue-shift agrees well with what we obtain from the SHG measurement, which supports our assumption that the initial strain is purely uniaxial. As the calculation of the photoelastic parameters depends on the strain derivation of the fit parameters A and B, initial strain does not alter the relative magnitude between p_1 and p_2. However, the relation between the photoelastic parameters and $\chi_0^{(2)}$ is affected by initial strain and has to be considered. As long as the initial strain coordinate system is parallel or perpendicular to the applied strain direction, the initial strain simply adds to the applied strain. In the $MoSe_2$ sample, the compressive initial strain is perpendicular to the tensile applied strain and both contributions amplify each other [see Fig. 2(b)]. On the contrary, when the sample is rotated by 90° [Fig. 2(j)], the initial strain and applied strain are parallel and the tensile applied strain compensates the compressive initial strain. Then the initially broken symmetry can be restored by applying strain. In the MoS_2 sample, the initial strain is small and the broken symmetry of the SHG measurement at zero applied strain was not recognized while taking the SHG measurements. The sample was thus not oriented parallel or perpendicular to the applied strain, resulting in an offset of the uniaxial strain direction θ for the first few measurement points [see Fig. 3(i)]. But since this offset is quickly vanishing with the applied strain (because the initial strain in this sample is small), the influence of the initial strain is negligible. The obtained $p_1/\chi_0^{(2)}$ and $p_2/\chi_0^{(2)}$ values agree well with our previous report[35] where a different transfer technique, a bending system, and a fitting process were used.

For WSe_2, the six-fold SHG symmetry is not broken, and we are thus not able to extract the initial strain from the SHG experiment. However, we can use the blue-shift of the A-exciton position (ΔE_g = 15 meV, with an unstrained A-exciton peak position at 1.65 eV[48]) and get a corresponding initial strain of −0.28%, similar to that of the other materials. The fitted strain direction θ for WSe_2 originates from the SHG setup and reflects the unavoidable but small polarization anisotropy. The relatively large error-bars of this fit parameter emphasize the weak influence of the polarization anisotropy.

In MoS_2, $MoSe_2$, and WS_2 monolayers, the symmetry reduction of uniaxial strain is strongly reflected in the polarization-resolved SHG patterns. In contrast, the relative size of the SHG petals do not change in WSe_2 monolayers. This implies that for WSe_2 the difference between p_1 and p_2 is approximately zero. This is confirmed, within the error margins, by the parameters extracted from the fitting process. The numerical values of the sum and difference of the photoelastic tensor elements can be found in Table II. For MoS_2 and WS_2, the term $p_1 - p_2$ is positive which means that the SHG, under increasing uniaxial strain, is increased parallel to the uniaxial strain direction and decreased perpendicular to the uniaxial strain direction. The sum of p_1 and p_2 is negative for MoS_2 and WS_2 which implies that the overall SHG intensity gets smaller with increasing strain. For MoS_2, the SHG increase along the uniaxial strain direction due to the difference of p_1 and p_2 and the overall decrease in SHG caused by the negative sum of p_1 and p_2 balances out perfectly, which means that in the uniaxial strain direction the SHG intensity remains constant. In other words, the strain gradient of the A and B fit parameters has the same magnitude and opposite signs. This behavior was observed before and used as a constraint in order to fit the photoelastic parameters.[35] In WS_2, this correlation is not observed. There, the overall SHG intensity is slightly shrinking with increasing strain, but it is growing along the uniaxial strain direction. For $MoSe_2$, the SHG evolution with increasing strain is the most prominent. The term $p_1 - p_2$ is negative, which implies that under increasing uniaxial strain the SHG intensity is increasing perpendicular to the uniaxial strain direction and decreasing in the parallel direction. The SHG growth perpendicular to the uniaxial strain direction outweighs the overall shrinking, caused by the negative sum of p_1 and p_2. WSe_2 has, in contrast to all other investigated materials, a positive sum of its photoelastic parameters. For this reason, the SHG increases in all polarization directions under tensile strain.

The question why the SHG is so sensitive to strain and why the SHG is unique for each material remains open. We speculate that excitonic effects may play an important role. This hypothesis is supported by the fact that the frequency-doubled photon energy is close to the C-exciton resonance of the investigated TMD samples. Wavelength-dependent measurements are currently performed to confirm this hypothesis and will be reported elsewhere.

TABLE II. Numerical values of the sum and difference of the photoelastic tensor parameters p_1 and p_2 for the investigated materials.

	MoS_2	$MoSe_2$	WS_2	WSe_2
$\frac{1}{\chi_0^{(2)}}(p_1 - p_2)$ (1/%)	0.44 ± 0.02	−0.96 ± 0.06	0.23 ± 0.03	−0.002 ± 0.02
$\frac{1}{\chi_0^{(2)}}(p_1 + p_2)$ (1/%)	−0.71 ± 0.02	−1.23 ± 0.06	−0.04 ± 0.03	0.32 ± 0.02

© Author(s) 2018

VI. CONCLUSION

In summary, we experimentally determined the second-order nonlinear photoelastic tensors of MoS_2, $MoSe_2$, WS_2, and WSe_2 at 800 nm excitation wavelength. Even under small strains, the SHG response changes considerably and the behavior under strain is unique for each material. In the course of this analysis, we also determined the relative SHG intensity of these materials. Furthermore, we observed that the PDMS based exfoliation and transfer of TMD monolayers leads to a uniaxial strain of around 0.2%. The photoelastic tensor elements can be used to measure strain maps via polarization-resolved SHG. At 800 nm excitation, p_1 and p_2 are equal in WSe_2. This is unique among the investigated materials and implies that (at this wavelength) no distinct strain tensor determination via polarization-resolved SHG is possible.

ACKNOWLEDGMENTS

We are grateful to Florian Libisch, Valerie Smejkal, Lukas Linhart, and Marco M. Furchi for helpful discussions. We acknowledge financial support by the European Union (Grant Agreement No. 785219 Graphene Flagship), the Austrian Science Fund FWF (START Y 539-N16), and the doctoral college program "TU-D Unravelling advanced 2D materials" funded by TU Vienna.

REFERENCES

[1] P. A. Franken, A. E. Hill, C. W. Peters, and G. Weinreich, "Generation of optical harmonics," Phys. Rev. Lett. **7**, 118 (1961).
[2] R. H. Stolen, J. E. Bjorkholm, and A. Ashkin, "Phase-matched three-wave mixing in silica fiber optical waveguides," Appl. Phys. Lett. **24**, 308 (1974).
[3] J. Kerr, "A new relation between electricity and light: Dielectrified media birefringent," London, Edinburgh Dublin Philos. Mag. J. Sci. **50**, 337–348 (1875).
[4] W. R. Bosenberg, A. Drobshoff, J. I. Alexander, L. E. Myers, and R. L. Byer, "93% pump depletion, 3.5-W continuous-wave, singly resonant optical parametric oscillator," Opt. Lett. **21**, 1336–1338 (1996).
[5] Y. Shih, "Entangled biphoton source–Property and preparation," Rep. Prog. Phys. **66**, 1009–1044 (2003).
[6] D. E. Spence, P. N. Kean, and W. Sibbett, "60-fsec pulse generation from a self-mode-locked Ti:sapphire laser," Opt. Lett. **16**, 42–44 (1991).
[7] Y. R. Shen, *The Principles of Nonlinear Optics* (John Wiley & Sons, NY, 1984).
[8] K. S. Novoselov *et al.*, "Two-dimensional atomic crystals," Proc. Natl. Acad. Sci. U. S. A. **102**, 10451–10453 (2005).
[9] K. F. Mak, K. He, J. Shan, and T. F. Heinz, "Control of valley polarization in monolayer MoS_2 by optical helicity," Nat. Nanotechnol. **7**, 494–498 (2012).
[10] A. Lipatov, P. Sharma, A. Gruverman, and A. Sinitskii, "Optoelectrical molybdenum disulde (MoS_2)-ferroelectric memories," ACS Nano **9**, 8089–8098 (2015).
[11] H. Zhu, Y. Wang, J. Xiao, M. Liu, S. Xiong, Z. J. Wong, Z. Ye, Y. Ye, X. Yin, and X. Zhang, "Observation of piezoelectricity in free-standing monolayer MoS_2," Nat. Nanotechnol. **10**, 151 (2015).
[12] A. Chernikov *et al.*, "Exciton binding energy and nonhydrogenic Rydberg series in monolayer WS_2," Phys. Rev. Lett. **113**, 076802 (2014).
[13] N. Kumar, S. Najmaei, Q. Cui, F. Ceballos, P. M. Ajayan, J. Lou, and H. Zhao, "Second harmonic microscopy of monolayer MoS_2," Phys. Rev. B **87**, 161403R (2013).
[14] L. M. Malard, T. V. Alencar, A. P. M. Barboza, K. F. Mak, and A. M. de Paula, "Observation of intense second harmonic generation from MoS_2 atomic crystals," Phys. Rev. B **87**, 201401R (2013).
[15] Y. Li, Y. Rao, K. F. Mak, Y. You, S. Wang, C. R. Dean, and T. F. Heinz, "Probing symmetry properties of few-layer MoS_2 and h-BN by optical second-harmonic generation," Nano Lett. **13**, 3329–3333 (2013).
[16] Y. R. Shen, "Optical second harmonic generation at interfaces," Annu. Rev. Phys. Chem. **40**, 327–350 (1989).
[17] R. I. Woodward *et al.*, "Characterization of the second- and third-order nonlinear optical susceptibilities of monolayer MoS_2 using multiphoton microscopy," 2D Mater. **4**, 11006 (2016).
[18] K. Liu, L. Zhang, T. Cao, C. Jin, D. Qiu, Q. Zhou, A. Zettl, P. Yang, S. G. Louie, and F. Wang, "Evolution of interlayer coupling in twisted molybdenum disulfide bilayers," Nat. Commun. **5**, 4966 (2014).
[19] X. Yin, Z. Ye, D. A. Chenet, Y. Ye, K. O'Brien, J. C. Hone, and X. Zhang, "Edge nonlinear optics on a MoS_2 atomic monolayer," Science **344**, 6183 (2014).
[20] L. Karvonen *et al.*, "Rapid visualization of grain boundaries in monolayer MoS_2 by multiphoton microscopy," Nat. Commun. **8**, 15714 (2017).
[21] S. Bertolazzi, J. Brivio, and A. Kis, "Stretching and breaking of ultrathin MoS_2," ACS Nano **5**, 9703–9709 (2011).
[22] K. He, C. Poole, K. F. Mak, and J. Shan, "Experimental demonstration of continuous electronic structure tuning via strain in atomically thin MoS_2," Nano Lett. **13**, 2931–2936 (2013).
[23] C. Rice, R. J. Young, R. Zan, and U. Bangert, "Raman-scattering measurements and first-principles calculations of strain-induced phonon shifts in monolayer MoS_2," Phys. Rev. B **87**, 081307 (2013).
[24] I. Niehues *et al.*, "Strain control of exciton–phonon coupling in atomically thin semiconductors," Nano Lett. **18**, 1751–1757 (2018).
[25] A. Castellanos-Gomez, R. Roldán, E. Cappelluti, M. Buscema, F. Guinea, H. S. J. van der Zant, and G. A. Steele, "Local strain engineering in atomically thin MoS_2," Nano Lett. **13**, 5361–5366 (2013).
[26] P. Tonndorf *et al.*, "Single-photon emission from localized excitons in an atomically thin semiconductor," Optica **2**, 347 (2015).
[27] A. Srivastava *et al.*, "Optically active quantum dots in monolayer WSe_2," Nat. Nanotechnol. **10**, 491–496 (2015).
[28] Y.-M. He *et al.*, "Single quantum emitters in monolayer semiconductors," Nat. Nanotechnol. **10**, 497–502 (2015).
[29] M. Koperski *et al.*, "Single photon emitters in exfoliated WSe_2 structures," Nat. Nanotechnol. **10**, 503–506 (2015).
[30] C. Chakraborty, L. Kinnischtzke, K. M. Goodfellow, R. Beams, and A. N. Vamivakas, "Voltage-controlled quantum light from an atomically thin semiconductor," Nat. Nanotechnol. **10**, 507–511 (2015).
[31] T. T. Tran, K. Bray, M. J. Ford, M. Toth, and I. Aharonovich, "Quantum emission from hexagonal boron nitride monolayers," Nat. Nanotechnol. **11**, 37–41 (2015).
[32] S. E. Thompson *et al.*, "A 90-nm logic technology featuring strained-silicon," IEEE Trans. Electron Devices **51**, 1790–1797 (2004).
[33] M. Hosseini, M. Elahi, M. Pourfath, and D. Esseni, "Very large strain gauges based on single layer $MoSe_2$ and WSe_2 for sensing applications," Appl. Phys. Lett. **107**, 253503 (2015).
[34] M. Hosseini, M. Elahi, M. Pourfath, and D. Esseni, "Strain-induced modulation of electron mobility in single-layer transition metal dichalcogenides," IEEE Trans. Electron Devices **62**, 3192–3198 (2015).
[35] L. Mennel, M. M. Furchi, S. Wachter, M. Paur, D. K. Polyushkin, and T. Mueller, "Optical imaging of strain in two-dimensional crystals," Nat. Commun. **9**, 516 (2018).
[36] J. Liang *et al.*, "Monitoring local strain vector in atomic-layered $MoSe_2$ by second-harmonic generation," Nano Lett. **17**, 7539 (2017).
[37] U. Wurstbauer, B. Miller, E. Parzinger, and A. W. Holleitner, "Light–matter interaction in transition metal dichalcogenides and their heterostructures," J. Phys. D: Appl. Phys. **50**, 17 (2017).
[38] N. I. Zheludev, S. V. Popov, and Y. P. Svirko, *Susceptibility Tensors for Nonlinear Optics* (Institute of Physics Publishing, Bristol, 1995).

© Author(s) 2018

[39] I. L. Lyubchanskii, N. N. Dadoenkova, M. I. Lyubchanskii, T. Rasing, J.-W. Jeong, and S.-C. Shin, "Second-harmonic generation from realistic film substrate interfaces: The effects of strain," Appl. Phys. Lett. **76**, 1848 (2000).

[40] C. R. Zhu *et al.*, "Strain tuning of optical emission energy and polarization in monolayer and bilayer MoS_2," Phys. Rev. B **88**, 121301 (2013).

[41] S. Chung and S. Park, "Effects of temperature on mechanical properties of SU-8 photoresist material," J. Mech. Sci. Technol. **27**, 2701–2707 (2013).

[42] A. Castellanos-Gomez, M. Buscema, R. Molenaar, V. Singh, L. Janssen, H. S. J. van der Zant, and G. A. Steele, "Deterministic transfer of two-dimensional materials by all-dry viscoelastic stamping," 2D Mater. **1**, 011002 (2014).

[43] E. Jones, E. Oliphant, P. Peterson *et al.*, see http://www.scipy.org/ for SciPy: Open Source Scientific Tools for Python, 2001; accessed 28 June 2018.

[44] A. Jain, P. Bharadwaj, S. Heeg, M. Parzefall, T. Taniguchi, K. Watanabe, and L. Novotny, "Minimizing residues and strain in 2D materials transferred from PDMS," Nanotechnology **29**, 265203 (2018).

[45] J. Kang, S. Tongay, J. Zhou, J. Li, and J. Wu, "Band offsets and heterostructures of two-dimensional semiconductors," Appl. Phys. Lett. **102**, 012111 (2013).

[46] R. C. Cooper, C. Lee, C. A. Marianetti, X. Wei, J. Hone, and J. W. Kysar, "Nonlinear elastic behavior of two-dimensional molybdenum disulfide," Phys. Rev. B **87**, 035423 (2013).

[47] K. Liu *et al.*, "Elastic properties of chemical-vapor-deposited monolayer MoS_2, WS_2, and their bilayer heterostructures," Nano Lett. **14**, 5097 (2014).

[48] G. H. Ahn, M. Amani, H. Rasool, D.-H. Lien, J. P. Mastandrea, J. W. Ager III, M. Dubey, D. C. Chrzan, A. M. Minor, and A. Javey, "Strain-engineered growth of two-dimensional materials," Nat. Commun. **8**, 608 (2017).

© Author(s) 2018